Data Science in Science

ISSN: (Print) (Online) Journal homepage: www.tandfonline.com/journals/udss20

Assessment of Glioblastoma Multiforme Tumor Heterogeneity via MRI-Derived Shape and Intensity Features

Yi Tang Chen & Sebastian Kurtek

To cite this article: Yi Tang Chen & Sebastian Kurtek (2024) Assessment of Glioblastoma Multiforme Tumor Heterogeneity via MRI-Derived Shape and Intensity Features, Data Science in Science, 3:1, 2415690, DOI: 10.1080/26941899.2024.2415690

To link to this article: https://doi.org/10.1080/26941899.2024.2415690

DATA SCIENCE IN SCIENCE
2024, VOL. 3, NO. 1, 2415690
https://doi.org/10.1080/26941899.2024.2415690

Assessment of Glioblastoma Multiforme Tumor Heterogeneity via MRI-Derived Shape and Intensity Features

Yi Tang Chen and Sebastian Kurtek

Department of Statistics, The Ohio State University, Columbus, OH, USA

ABSTRACT

We use a geometric approach to jointly characterize tumor shape and intensity along the tumor contour, as captured in magnetic resonance images, in the context of glioblastoma multiforme. Key properties of the proposed shape + intensity representation include invariance to translation, scale, rotation and reparameterization, which enable objective characterization and comparison of these crucial tumor features. The representation further allows the user to tune the emphasis of the shape and intensity components during registration, comparison and statistical summarization (averaging, computation of overall variance and exploration of variability *via* principal component analysis). In addition, we define a composite distance that is able to integrate shape and intensity information from two imaging modalities. The proposed framework can be integrated with distance-based clustering for the purpose of discovering groups of subjects with distinct survival prognosis. When applied to a cohort of subjects with glioblastoma multiforme, we discover groups with large median survival differences. We further tie the subjects' cluster memberships to tumor heterogeneity. Our results suggest that tumor shape variation plays an important role in disease prognosis.

ARTICLE HISTORY
Received 4 March 2024
Revised 30 August 2024
Accepted 2 October 2024

KEYWORDS
Magnetic resonance image; glioblastoma multiforme; elastic distance; tumor heterogeneity; clustering; survival analysis

1. Introduction

Glioblastoma multiforme (GBM) is a severe type of brain cancer commonly found in adults (Holland 2000). The median survival time following diagnosis is approximately 12 months (McLendon et al. 2008), with fewer than 10% of subjects surviving five years after diagnosis (Tutt 2011). GBM is a morphologically heterogeneous disease that is often diagnosed and examined using magnetic resonance imaging (MRI). Imaging features derived from MRI, in particular the shape and intensity or texture of the brain tumor, have been recognized as relevant prognostic factors for GBM (Bharath et al. 2018; Saha et al. 2016). The shape of a GBM tumor can reveal the extent of infiltration of the tumor into surrounding tissues, while tumor intensity can capture properties of these tissues, e.g., edema or infiltrated tumor cells (Hawkins-Daarud et al. 2013; Zinn et al. 2011). Thus, both features of imaged GBM tumors are pivotal for evaluating disease severity.

However, there is a lack of reliable and objective characterization of GBM tumor shape and intensity for the purposes of their comparison and statistical modeling. Domain experts often represent tumor shape in ways that are only able to capture its partial geometric complexity, e.g., using subjective features such as irregularity, circularity, major axis length, etc. (Chaddad et al. 2016; Krabbe et al. 1997). Similarly, tumor intensity information is often transformed into a histogram, which is then used to derive simple features that can be incorporated into statistical models as GBM biomarkers, e.g., skewness, kurtosis, range, mode or percentiles (Baek et al. 2012; Just 2011; Song et al. 2013). Moreover, GBM tumor shape and intensity are often studied separately, potentially overlooking the interdependence between these two tumor signatures (Gevaert et al. 2014).

To address these deficiencies, we develop a geometric approach that integrates, and appropriately balances, information related to GBM tumor shape and intensity *via* a unified mathematical representation. The proposed representation and associated distance provide reliable characterization and facilitate objective comparison of GBM tumors. They further enable joint statistical analysis of shape and intensity features of MRI-derived GBM tumors. Bharath et al. (2018) defined and studied variation in GBM tumor shapes based on a parameterized curve representation under the elastic shape analysis framework (Srivastava and Klassen 2016). They showed that registration of GBM tumor outlines, *via* removal of nuisance variation related to translation, scale, orientation and parameterization from the shape representation space, resulted in more informative tumor comparisons, quantification of tumor shape heterogeneity and associated survival

CONTACT Sebastian Kurtek kurtek.1@stat.osu.edu Department of Statistics, The Ohio State University, 1958 Neil Ave, Columbus, OH 43210, USA
Supplemental data for this article can be accessed online at https://doi.org/10.1080/26941899.2024.2415690.

analysis. We build on their framework by additionally incorporating information about the intensity (texture) along tumor contours by defining a joint GBM tumor shape-+intensity representation. Our approach leads to a distance between shape and intensity features of GBM tumors that remains invariant to all shape and intensity preserving transformations. Importantly, it allows for joint registration of GBM tumor shape and intensity, thus capturing their interdependence. The proposed distance for comparison of GBM tumor shape + intensity can then be employed for assessing and visualizing tumor heterogeneity *via* statistical summarization (mean computation and principal component analysis), clustering and survival analysis. We show that joint statistical analysis of GBM tumor shape + intensity results in enhanced quantification of tumor heterogeneity by identifying groups of subjects, *via* (unsupervised) hierarchical clustering, with distinct survival profiles. We also present results that relate other covariates, in particular sex of subjects, to GBM tumor shape + intensity characteristics.

While the proposed GBM tumor shape + intensity representation was introduced in Chen and Kurtek (2023) and is similar in spirit to the representation defined in Liu et al. (2008), this manuscript presents significant extensions as well as a more comprehensive statistical analysis of a GBM tumor dataset. Our contributions, beyond Chen and Kurtek (2023); Liu et al. (2008), are as follows.

- We define methods for joint statistical summarization of GBM tumor shape and intensity heterogeneity via a mean, measure of overall variance and exploration of dominant modes of variability using principal component analysis.
- We define a composite distance that is able to integrate GBM tumor shape + intensity information from two MRI modalities.
- We use the defined distances for partitioning of subjects with GBM into groups with distinct survival profiles. We then quantify and visualize GBM tumor shape + intensity heterogeneity within these clusters. We discover a consistent trend wherein clusters with shorter median survival contain GBM tumors that are more heterogeneous.

1.1. Dataset Description and Pre-Processing

We obtained magnetic resonance images and associated covariates, including age, gender, tumor volume (in voxels), survival status and survival time (in months), for 63 subjects diagnosed with GBM who consented under the Cancer Genome Atlas protocols[1], from the Cancer Imaging Archive[2]. Table 1 shows summary statistics for different subject characteristics. In this study, we consider MRI data from two modalities: T1-weighted post contrast, henceforth referred to as T1, and T2-FLAIR, henceforth referred to as FLAIR. Preprocessing of the data, e.g., segmentation of tumors from MRI images, followed a standard pipeline for structural MRI and is described in detail in Saha et al. (2016). In brief, preprocessing involved (i) registration of FLAIR images to corresponding T1 images, (ii) inhomogeneity correction of FLAIR and T1 images, (iii) semi-automatic segmentation of the tumors using the Medical Image Interaction Toolkit MITK3M3 Image Analysis (v1.1.0) and the NIFTI toolbox in MATLAB. In T1, the segmented region corresponds to the contrast enhancing tumor. In FLAIR, the segmented region corresponds to the solid tumor, and regions of edema and infiltrating tumor (Saha et al. 2016). In similar fashion to Bharath et al. (2018) and Saha et al. (2016), our study focuses on the analysis of GBM tumor shape + intensity captured in the axial image slice with the largest tumor area in the T1 modality, and the corresponding slice in the FLAIR modality that has the same anatomical vertical position. Figure 1(a) shows an example of such a T1 axial slice for one subject with GBM, while Figure 1(b) shows the corresponding FLAIR axial slice. The segmented tumor outlines are illustrated as red contours that are overlaid on the images. Noticeably, the appearance of the tumor outlines differs across the two MRI modalities even though the images are for the same subject. This is because different MRI modalities highlight different tissue properties: T1 highlights fat tissues while FLAIR highlights not only fat tissues, but also structures with high water content. Consequently, the tumor contour in the T1 image captures the solid tumor area, whereas the tumor contour in the FLAIR image captures the solid tumor area as well as regions of edema in the surrounding tissues.

Table 1. Summary statistics of GBM subject characteristics.

Variable	Categorical level	Numerical summary
Age (mean (SD))		56.33 (15.44)
Gender (*n* (%))	Female	21 (33.3)
	Male	42 (66.7)
Survival status (*n* (%))	Deceased	57 (90.5)
	Living	6 (9.5)
Survival time (med (IQR))		13.6 (6.87, 26.40)
FLAIR volume (mean (SD))		135,953.38 (88,272.70)
T1 volume (mean (SD))		128,692.81 (90,581.05)

We use SD for standard deviation, n for sample size, med for median and IQR for interquartile range.

The rest of this paper is organized as follows. Section 2 presents details of the statistical framework for shape-+intensity analysis of GBM tumors. First, in Section 2.1, we introduce the mathematical representation and distance for comparison of shape + intensity based on a single MRI modality. In Section 2.2, these are further used to define tools for (i) averaging, (ii) quantification of overall variation, and (iii) exploration of dominant modes of variability of GBM tumor shape + intensity features. Finally, in Section 2.3, we specify a composite distance that is able to integrate shape + intensity information from two MRI modalities. Section 3 describes a comprehensive application of the proposed statistical analysis tools on the GBM tumor dataset described in Section 1.1. Our focus in this section is on assessment of GBM tumor shape + intensity heterogeneity and how it relates to other covariates, e.g., sex (Section 3.2) and survival time (Section 3.3). We close with a brief discussion and directions for future work in Section 4.

The Supplementary Materials contain (i) a study to determine an appropriate sampling density for shape + intensity in each modality (Section S1), (ii) software implementation details (Section S2), (iii) description of algorithms (Section S3), (iv) description of the data generating process for

simulated shape + intensity (Section S4), (v) a procedure for bootstrap estimation of variance for average shape + intensity (Section S5), (vi) a procedure for distance-based outlier detection (Section S6), (vii) additional details of comparative analyses (Section S7), (viii) distance-based classification studies using shape + intensity (Section S8), and (ix) alternative displays of shape + intensity principal directions of variation (Section S9).

2. Methodology

We begin by defining a mathematical representation of image-derived GBM tumors, which captures their shape and intensity information. We refer to this representation as shape + intensity for simplicity of presentation. We then specify an elastic distance for comparison of GBM tumor shape + intensity, which allows for registration of these features with respect to rotation and reparameterization. The distance is used to further define procedures for averaging of and assessing variability in a sample of GBM tumor shape + intensity. Finally, we define a composite elastic distance that allows for integration of shape + intensity information from two imaging modalities. The proposed framework builds on tools from elastic shape analysis (Chen and Kurtek 2023; Liu et al. 2008; Srivastava and Klassen 2016). Throughout this manuscript, we use $|\cdot|$ and $||\cdot||$ to denote the Euclidean norm in $\mathbb{R}^3$ and the $\mathbb{L}^2$ norm, respectively.

2.1. GBM Tumor Shape + Intensity Representation and Distance

We first construct a coordinate function that consists of (i) the x and y coordinate functions of the tumor outline, and (ii) the intensity function along the tumor outline. Let $\beta_c : \mathbb{S}^1 \to \mathbb{R}^2$ denote the 2D closed curve representing the tumor outline, and $\beta_I : \mathbb{S}^1 \to \mathbb{R}$ denote the intensity function along the tumor outline. As seen in Figure 1, segmented GBM tumor contours, as well as the associated intensity functions, form closed curves, making the unit circle domain $\mathbb{S}^1$ a natural choice in this application. Motivated by the discrete nature of MRI data, we take the following pre-processing steps to construct β_c and β_I from segmented images. To obtain β_c, we smooth each tumor outline, which is originally represented by discrete x and y image coordinates, using a five-point moving average smoother. Then, the intensity value at each point on β_c is obtained by taking the average of the five intensity values at the discrete x and y image coordinates that are closest (with respect to the Euclidean distance) to the x and y coordinate on β_c. This averaging step serves two purposes: (i) it mitigates effects of potential noise in the intensity values, and (ii) it allows us to incorporate intensity information from tissues that surround the tumor outline. We then additionally smooth the intensity function using cubic splines to obtain β_I.

We rescale β_c to unit length to remove scaling variability in the eventual shape component of the proposed representation. We denote the rescaled β_c by β_c^*, where $\int_{\mathbb{S}^1} |\dot{\beta}_c^*(t)| dt = 1$ ($\dot{\beta}_c^*$ denotes the coordinatewise derivative of β_c^*). In case the size of GBM tumors is also of interest, one may choose to not normalize the scale of their outlines, leading to size-and-shape analysis (Kurtek et al. 2012). In our analyses, we remove this source of variation since there exist significant tumor size differences across GBM subjects. Such scale differences can result in tumor comparisons that are primarily driven by their size, consequently overlooking important geometric differences in shape, e.g., regions of protrusion. Furthermore, tumor volume, one of the variables in the dataset, can be incorporated separately into any statistical analysis task of interest. The intensity function β_I is also standardized by subtracting its average and dividing by its standard deviation (Ellingson et al. 2012). This is motivated by a well-known issue that arises in MRI studies, where intensity values corresponding to the same or similar

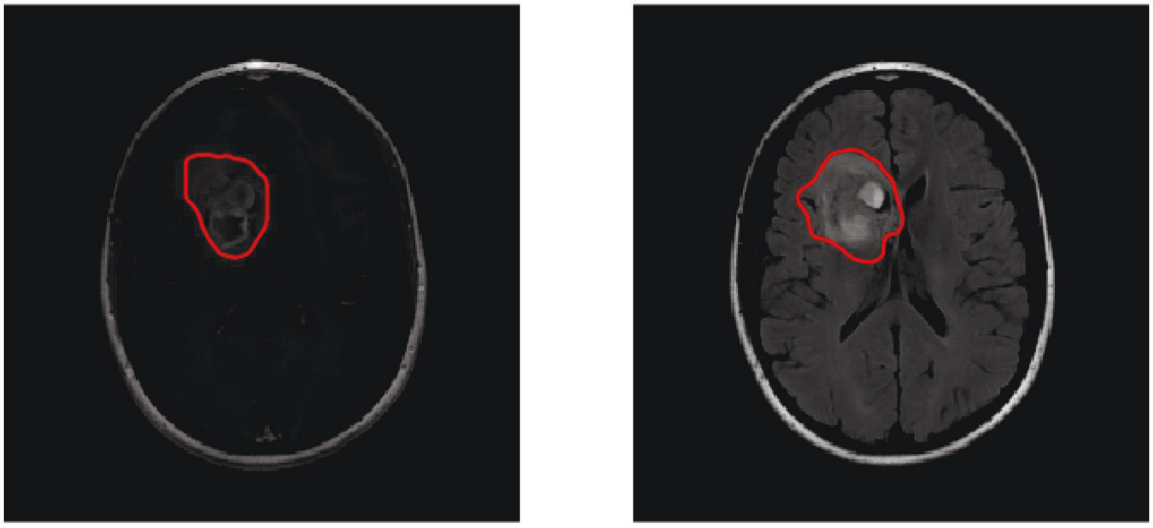

(a) (b)

Figure 1. (a) T1 axial image slice with largest tumor area and (b) corresponding FLAIR slice for a GBM subject in the dataset with survival time of 12.2 months. The tumor outline is highlighted as a red contour and overlaid on each image.

tissues can vary across images/subjects, making them not directly comparable (Nyúl and Udupa 1999). The standardized β_I is denoted by β_I^*. We then define $\beta_\lambda^* = \begin{bmatrix} \beta_c^* \\ \lambda\beta_I^* \end{bmatrix} : \mathbb{S}^1 \to \mathbb{R}^3$, where β_I^* is additionally scaled by a parameter $\lambda \in \mathbb{R}_+$, which controls the emphasis of intensity information in the proposed representation. Thus, we model each tumor outline, and the intensity along the outline, as a three-dimensional parameterized closed curve. A pictorial illustration of the construction of β_λ^* (for $\lambda = 1$) based on a segmented MRI image of a GBM tumor is presented in Figure 2.

The defined tumor representation, β_λ^*, contains two additional sources of nuisance variation: (i) orientation or rotation of the tumor contour in the image, and (ii) parameterization of the tumor contour and intensity function. In order to define a shape + intensity representation based on β_λ^*, we must thus account for these two additional sources of variability. For rotations, our focus is on a subgroup of $SO(3)$, $R = \begin{bmatrix} SO(2) & 0 \\ 0 & 1 \end{bmatrix} \subset SO(3)$, elements of which rotate the first two (tumor contour) coordinates of β_λ^*, but not the third (intensity) coordinate. The rotation of β_λ^* by $O \in R$ is then given by the left group action of matrix multiplication: $O\beta_\lambda^*$. Different parameterizations of the closed curve β_λ^* involve (i) different seeds or starting points on the domain $\mathbb{S}^1$, and (ii) different speeds of traversal along the curve. Let $\Gamma = \{\gamma : \mathbb{S}^1 \to \mathbb{S}^1 | \gamma$ is an orientation preserving diffeomorphism$\}$ denote the group of reparameterization functions. Then, a reparameterization of β_λ^* by $\gamma \in \Gamma$ is given by the value-preserving group action of composition: $(\beta_\lambda^*, \gamma) = \beta_\lambda^* \circ \gamma$. In the applied context of capturing GBM tumor shape + intensity heterogeneity, the actions of R and Γ do not change the shape of the tumor outline, and must be appropriately removed from the representation space. At the same time, allowing flexible rotations and reparameterizations of β_λ^* results in optimal registration of geometric features of the tumor outline (eg regions of protrusion) and intensity function (eg local extrema) across GBM tumors. This results in more natural shape + intensity comparisons that preserve such features. We demonstrate this later in Section 3.

To remove the rotation and parameterization variabilities, we seek a rotation- and parameterization-invariant distance $d(\cdot,\cdot)$ between two closed curves $\beta_{\lambda,1}^*$ and $\beta_{\lambda,2}^*$, which must satisfy the isometry property:

$$d(\beta_{\lambda,1}^*, \beta_{\lambda,2}^*) = d(O(\beta_{\lambda,1}^* \circ \gamma), O(\beta_{\lambda,2}^* \circ \gamma)). \tag{1}$$

While convenient because of computational efficiency, it is well-known that the standard $\mathbb{L}^2$ distance does not satisfy this property (Srivastava and Klassen 2016). Instead, we use an elastic Riemannian metric, which is known to be (rotation- and) parameterization-invariant (Mio et al. 2007). The metric is called elastic as it measures the amount of bending and stretching/compression needed to deform one shape into another. The resulting Riemmanian distance can be computed efficiently using a convenient transformation called the square-root velocity function (SRVF), which flattens the elastic Riemannian metric to the $\mathbb{L}^2$ metric[3] (Kurtek et al. 2012; Srivastava et al. 2011). The SRVF of a curve β_λ^* is also a curve in $\mathbb{R}^3$ and is given by.

$$q_\lambda^* = \frac{\dot{\beta}_\lambda^*}{\sqrt{|\dot{\beta}_\lambda^*|}} : \mathbb{S}^1 \to \mathbb{R}^3, \tag{2}$$

where again $\dot{\beta}_\lambda^*$ denotes the coordinate wise derivative of β_λ^*. If the curve β_λ^* is absolutely continuous, then its SRVF q_λ^* is

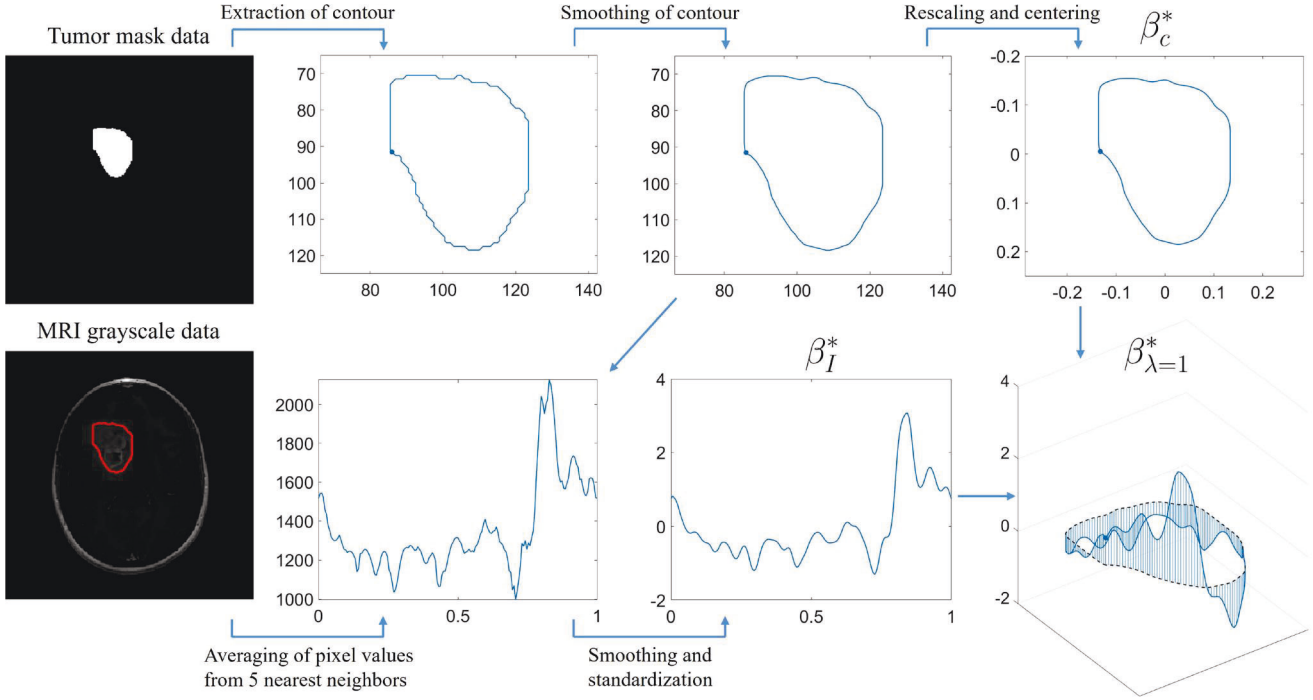

Figure 2. Flowchart illustrating construction of β_λ^* using a segmented MRI image of a GBM tumor.

an element of $\mathbb{L}^2(\mathbb{S}^1, \mathbb{R}^3)$ (Robinson 2012). Note that the SRVF representation is automatically invariant to translation as its definition only involves the derivative of β^*_λ. While the location of the tumor in the brain can potentially carry information about severity of GBM, our focus is on tumor shape + intensity heterogeneity and we thus remove this source of variation from the representation. As in the case of the size of the tumor, this information can be incorporated separately into statistical analyses. This leads to the definition of the pre-shape + intensity space of GBM tumors as the space of SRVFs of closed 3D curves: $\mathcal{C} = \{q^*_\lambda : \mathbb{S}^1 \to \mathbb{R}^3 \big| \int_{\mathbb{S}^1} q^*_\lambda(t)|q^*_\lambda(t)|dt = 0\}$. Because of the closure condition $\int_{\mathbb{S}^1} q^*_\lambda(t)|q^*_\lambda(t)|dt = 0$, $\mathcal{C}$ is non-linear leading to an intrinsic distance, induced from the $\mathbb{L}^2$ distance on $\mathbb{L}^2(\mathbb{S}^1, \mathbb{R}^3)$, that cannot be computed in closed form. Thus, for computational efficiency, we instead use the extrinsic $\mathbb{L}^2$ distance on the pre-shape + intensity space $\mathcal{C}$ given by (for $q^*_{\lambda,1}, \ q^*_{\lambda,2} \in \mathcal{C}$)

$$d_{\mathcal{C}}(q^*_{\lambda,1}, q^*_{\lambda,2}) = ||q^*_{\lambda,1} - q^*_{\lambda,2}||. \tag{3}$$

Importantly, as stated earlier, for a $\gamma \in \Gamma$ and $O \in R$, the $\mathbb{L}^2$ distance between two SRVFs $q^*_{\lambda,1}, \ q^*_{\lambda,2} \in \mathcal{C}$ is isometric under the actions of Γ and R:

$$\begin{aligned} &d_{\mathcal{C}}(q^*_{\lambda,1}, q^*_{\lambda,2}) = ||q^*_{\lambda,1} - q^*_{\lambda,2}|| = ||O(q^*_{\lambda,1}, \gamma) - O(q^*_{\lambda,2}, \gamma)|| \\ &= d_{\mathcal{C}}(O(q^*_{\lambda,1}, \gamma), O(q^*_{\lambda,2}, \gamma)). \end{aligned} \tag{4}$$

Here, we use the following two facts. First, a rotation of a curve β^*_λ by $O \in R$, $O\beta^*_\lambda$, corresponds to a rotation of its SRVF q^*_λ, Oq^*_λ. Second, a reparameterization of a curve β^*_λ by $\gamma \in \Gamma$, $\beta^*_\lambda \circ \gamma$, corresponds to the following transformation of its SRVF $q^*_\lambda : (q^*_\lambda, \gamma) = (q^*_\lambda \circ \gamma)\sqrt{\dot{\gamma}}$.

Since $d_{\mathcal{C}}(\cdot, \cdot)$ satisfies the isometry property with respect to rotations and reparameterizations, we use it to remove rotation and reparameterization variabilities from the representation space. Formally, we account for rotation and reparameterization variabilities in the representation q^*_λ (β^*_λ) *via* the definition of an orbit

$$[q^*_\lambda] = \{O(q^*_\lambda \circ \gamma)\sqrt{\dot{\gamma}} | \gamma \in \Gamma, \ O \in R\}, \tag{5}$$

which unifies all SRVFs within a rotation and reparameterization of each other. In other words, the entire orbit (set) $[q^*_\lambda]$ associated with q^*_λ represents the unique shape + intensity for a GBM tumor. The set of all such orbits is denoted by $\mathcal{S} = \{[q^*_\lambda] | q^*_\lambda \in \mathcal{C}\} = \mathcal{C}/(R \times \Gamma)$ and forms the shape + intensity quotient space. The shape + intensity space $\mathcal{S}$ is formed by partitioning the pre-shape + intensity space $\mathcal{C}$ *via* the orbits. The resulting distance between two shape + intensity orbits, $[q^*_{\lambda,1}], \ [q^*_{\lambda,2}] \in \mathcal{S}$, is defined *via* the $\mathbb{L}^2$ distance on $\mathcal{C}$ as follows:

$$\begin{aligned} d_{\mathcal{S}}([q^*_{\lambda,1}], [q^*_{\lambda,2}]) &= \inf_{O \in R, \ \gamma \in \Gamma} d_{\mathcal{C}}(q^*_{\lambda,1}, O(q^*_{\lambda,2} \circ \gamma)\sqrt{\dot{\gamma}}) \\ &= \inf_{O \in R, \ \gamma \in \Gamma} ||q^*_{\lambda,1} - O(q^*_{\lambda,2} \circ \gamma)\sqrt{\dot{\gamma}}||. \end{aligned} \tag{6}$$

The optimization problems over R and Γ are solved using Procrustes analysis, i.e., singular value decomposition (optimal rotation) (Dryden and Mardia 2016, Chapter 4), and the dynamic programming algorithm (Bertsekas 1995; Robinson 2012, Chapter 3) with an additional seed search (optimal reparameterization), respectively. A detailed algorithm for solving the optimization problem in Equation (6) is provided in Section S3.1 in the Supplementary Materials. This process aligns or registers the shape + intensity representations of GBM tumors such that the $\mathbb{L}^2$ distance between them is minimized. This, in turn, results in improved comparisons of GBM tumor shape + intensity features. Since similar geometric structure of tumor contours as well as similar intensity values along tumor contours can be indicative of similar tissue properties surrounding the infiltrating tumors, registration of tumor shape + intensity is necessary. In essence, this process allows matching of similar tissue properties across GBM tumors. Another important property of the defined shape + intensity distance is that the contribution of geometric contour information versus intensity information depends on the chosen value of λ in the representation. When λ is small, registration is driven primarily by geometric features of tumor contours, and when λ is large, it is driven by intensity information. We can visualize the geodesic path or optimal path of deformation between two GBM tumor shape + intensity objects *via* a linear interpolation between $q^*_{\lambda,1}$ and the optimally rotated and reparameterized $q^*_{\lambda,2}$,

$$(1-\tau) \ q^*_{\lambda,1} + \tau \ O^*(q^*_{\lambda,2} \circ \gamma^*)\sqrt{\dot{\gamma}^*}, \quad \tau \in [0,1], \tag{7}$$

where O^* and γ^* are the optimal rotation and reparameterization computed using Equation (6). The length of this path is given by $d_{\mathcal{S}}([q^*_{\lambda,1}], [q^*_{\lambda,2}])$. Such deformation paths provide insight into the contribution of the shape and intensity components in the registration and comparison of GBM tumors.

An illustration of registration and shape + intensity distance computation is provided in Figure 3. The two pre-shape + intensity objects in this figure were simulated using the data generating mechanism described in Section S4 in the Supplementary Materials. In the figure, the SRVFs of the two simulated pre-shape + intensity objects are represented by the two points labeled $q^*_{\lambda,1}$ and $q^*_{\lambda,2}$. They are elements of the pre-shape + intensity space $\mathcal{C}$ and lie in their respective orbits $[q^*_{\lambda,1}]$ and $[q^*_{\lambda,2}]$. The oribts are shown as two parallel straight lines to illustrate the fact that the distance $d_{\mathcal{C}}(\cdot, \cdot)$ is unchanged by a common rotation and/or reparameterization of the two pre-shape + intensity objects. In other words, applying a rotation $O \in R$ and a reparameterization $\gamma \in \Gamma$ to both $q^*_{\lambda,1}$ and $q^*_{\lambda,2}$ shifts these two points by the same amount along their orbits. Also, recall that all points lying along an orbit of a pre-shape + intensity object q^*_λ are equivalent representations of its shape + intensity. When visualized in the shape + intensity space $\mathcal{S}$, an entire orbit collapses to a single point. Then, the distance between two orbits on $\mathcal{S}$, each representing a unique tumor shape + intensity, can be computed on $\mathcal{C}$ by fixing an element in the first orbit and minimizing the distance $d_{\mathcal{C}}(\cdot, \cdot)$ over all elements of the second orbit. The minimizing distance is illustrated by the horizontal line that is orthogonal to the two parallel lines representing the orbits. For this particular example, we chose a very small value of $\lambda = 0.01$. Thus, registration primarily focuses on aligning geometric

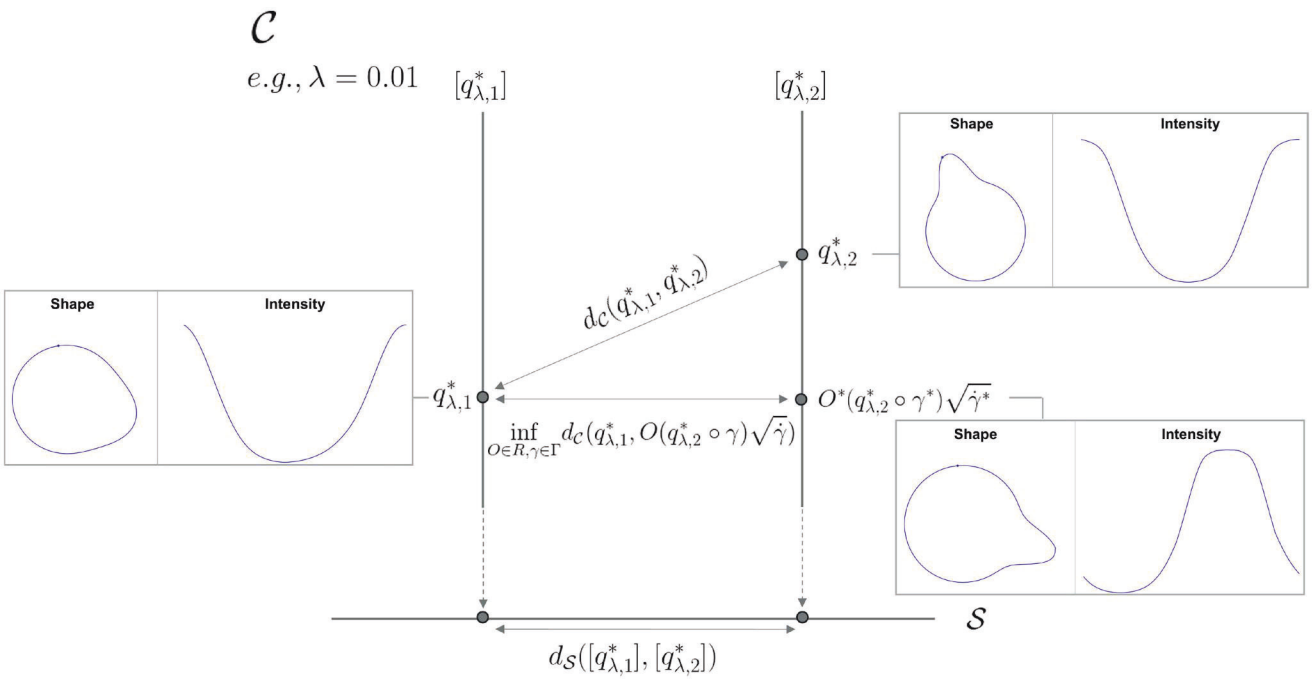

Figure 3. Illustration of registration and shape + intensity distance computation for two simulated pre-shape + intensity objects.

shape features. A more thorough discussion of the effects of λ on registration and subsequent shape + intensity distance computation will follow in Section 3.1.

2.2. Statistical Summarization of GBM Tumor Shape + Intensity

The proposed representation and distance enable joint statistical analysis of GBM tumor shape + intensity. Our focus here is on the definition and computation of an average, and exploration of variability *via* principal component analysis, based on a sample. Given $\beta^*_{\lambda,1}, ..., \beta^*_{\lambda,n}$, and their corresponding SRVFs $q^*_{\lambda,1}, ..., q^*_{\lambda,n}$, the sample shape + intensity average, for a fixed value of λ, is defined as

$$[\hat{\mu}_{\lambda,q}] = \arg\min_{[q] \in \mathcal{S}} \frac{1}{n} \sum_{i=1}^{n} d_{\mathcal{S}}([q], [q^*_{\lambda,i}])^2, \tag{8}$$

based on the distance $d_{\mathcal{S}}(\cdot, \cdot)$ defined in Equation (6). This optimization problem is solved using a gradient descent algorithm (Karcher 1977), the details of which are presented in Section S3.2 in the Supplementary Materials. Note that $[\hat{\mu}_{\lambda,q}]$ denotes an entire orbit, but we choose a single element $\hat{\mu}_{\lambda,q} \in [\hat{\mu}_{\lambda,q}]$ as its representative for visualization and subsequent analyses. To visualize the mean shape + intensity, we apply the inverse SRVF transformation: $\hat{\mu}_{\lambda}(t) = \int_0^t \hat{\mu}_{\lambda,q}(u)|\hat{\mu}_{\lambda,q}(u)|du$. One can further estimate the uncertainty of the sample shape + intensity average using the bootstrap. The procedure to compute the bootstrap estimate of variance for the sample shape + intensity average is described in Section S5 in the Supplementary Materials. Moreover, shape + intensity distances from the sample average can be used for outlier detection. Section S6 in the Supplementary Materials provides the procedure for outlier detection and describes associated results for the GBM dataset. Finally, the quantity

$$\hat{\rho}_{\lambda} = \frac{1}{n} \sum_{i=1}^{n} d_{\mathcal{S}}([\hat{\mu}_{\lambda,q}], [q^*_{\lambda,i}])^2 \tag{9}$$

is the overall variance in the shape + intensity sample, and can be used as a surrogate measure of GBM tumor heterogeneity.

Given an average shape + intensity, we can summarize and visualize variation *via* principal component analysis (PCA). First, each shape + intensity observation is registered to the average *via* Equation (6). With a slight abuse in notation, assuming that each registered SRVF $q^*_{\lambda,i}$, $i = 1, ..., n$ and the mean $\hat{\mu}_{\lambda,q}$ are sampled using T points, we compute $v_{\lambda,i} = q^*_{\lambda,i} - \hat{\mu}_{\lambda,q} \in \mathbb{R}^{3 \times T}$, $i = 1, ..., n$. Throughout the analyses presented in Section 3, we use $T = 180$ for T1 and $T = 280$ for FLAIR shape + intensity. These choices were informed by numerical precision of tumor contour length computations, which are described in Section S1 in the Supplementary Materials. We then concatenate the three coordinate vectors resulting in $\tilde{v}_{\lambda,i} \in \mathbb{R}^{3T}$, $i = 1, ..., n$, compute the sample covariance matrix $\hat{K}_{\lambda} = \frac{1}{n-1} \sum_{i=1}^{n} \tilde{v}_{\lambda,i} \tilde{v}_{\lambda,i}^{\top}$, and apply singular value decomposition $\hat{K}_{\lambda} = U \Sigma U'$. Then, we can visualize the sample shape + intensity variation within two standard deviations around the mean along the jth principal direction using the path,

$$\hat{\mu}_{\lambda,q} + s\sqrt{\Sigma_{jj}} U_j, \tag{10}$$

where Σ_{jj} is the jth diagonal element of Σ, U_j is the jth column of U and $s = -2, -1, 0, 1, 2$. Here, U_j is the jth primary direction of shape + intensity variation, Σ_{jj} is the variance along that direction, and the sample average corresponds to $s = 0$.

2.3. Multimodal Integration of GBM Tumor Shape + Intensity

In practice, clinicians often examine both the T1 and FLAIR modalities to draw conclusions about GBM severity since they highlight different tissue properties. To achieve joint comparisons of shape + intensity captured in T1 and FLAIR images, we leverage a product space structure to define a composite distance which integrates differences in T1 and FLAIR GBM tumor shape + intensity. Let $\mathcal{C}^j = \{q^{j*}_{\lambda_j} : \mathbb{S}^1 \to \mathbb{R}^3 | \int_{\mathbb{S}^1} q^{j*}_{\lambda_j}(t) | q^{j*}_{\lambda_j}(t) | dt = 0\}$ and $\mathcal{S}^j = \{[q^{j*}_{\lambda_j}]\}$ denote the pre-shape + intensity and shape + intensity spaces for the T1 ($j = 1$) and FLAIR ($j = 2$) MRI modalities, respectively, with orbits defined as in Section 2.1. Note that the parameters $\lambda_1, \lambda_2 \in \mathbb{R}_+$ can be different across the two modalities. Then, the composite shape + intensity distance on $\mathcal{P} = \mathcal{S}^1 \times \mathcal{S}^2$ is defined as (for $([q^{1*}_{\lambda_1,1}], [q^{2*}_{\lambda_2,1}]), ([q^{1*}_{\lambda_1,2}], [q^{2*}_{\lambda_2,2}]) \in \mathcal{P}$)

$$d_{\mathcal{P}}(([q^{1*}_{\lambda_1,1}], [q^{2*}_{\lambda_2,1}]), ([q^{1*}_{\lambda_1,2}], [q^{2*}_{\lambda_2,2}])) = \\ = \sqrt{(1-\alpha) d_{\mathcal{S}^1}([q^{1*}_{\lambda_1,1}], [q^{1*}_{\lambda_1,2}])^2 + \alpha \; d_{\mathcal{S}^2}([q^{2*}_{\lambda_2,1}], [q^{2*}_{\lambda_2,2}])^2}, \tag{11}$$

where $\alpha \in [0,1]$ is a weight that controls the emphasis of each of the modalities, and $d_{\mathcal{S}^j}([q^{j*}_{\lambda_j,1}], [q^{j*}_{\lambda_j,2}]) = \inf_{O_j \in R,\ \gamma_j \in \Gamma} ||q^{j*}_{\lambda_j,1} - O_j(q^{j*}_{\lambda_j,2} \circ \gamma_j)\sqrt{\dot{\gamma}_j}||$ for $j = 1, 2$. Small values of α allow comparisons to primarily focus on shape + intensity GBM tumor differences in the T1 modality. Similarly, large values of α put emphasis on the differences in the FLAIR modality. Importantly, the registration of shape + intensity, i.e., optimal rotation and reparameterization, can differ across the two modalities.

3. Assessment of GBM Tumor Shape + Intensity Heterogeneity

We apply the proposed framework to assess heterogeneity in MRI-derived GBM tumor shape + intensity features. We begin with illustrations of registration, comparison and optimal deformation for a simulated example and for multiple real GBM tumors. Next, we summarize shape + intensity variation by sex. We calculate group specific sample means and perform principal component analysis for different values of λ. Then, we describe the use of the proposed shape + intensity distances for clustering of GBM tumors, and relate our results to survival and tumor heterogeneity.

Throughout this section, the smallest value of λ that we consider is $\lambda = 0.01$. In this case, the majority of information comes from differences in GBM tumor shape. The largest value of λ that we consider is $\lambda = 0.5$ since the scale of the intensity values (after standardization) is larger than that of the GBM tumor contour coordinates (after rescaling to unit length). When $\lambda = 0.5$, intensity information dominates registration and comparison of GBM tumor shape + intensity. We found empirically that registration and comparison results for $\lambda > 0.5$ are very similar, if not the same, to those for $\lambda = 0.5$

When relating our results to survival, we estimate median survival time based on the Kaplan-Meier estimate of the survival function, which accounts for censoring in the subjects' survival times. One can also use other summaries of survival such as mean survival time, which can be estimated using the area under the Kaplan-Meier curve. We use median survival rather than mean survival, as the latter can be underestimated if the longest observation time is censored, which is often the case in GBM.

We provide software implementation details for the analyses presented here in Section S2 in the Supplementary Materials. Code to reproduce the analyses is also available as a separate supplement.

3.1. Registration, Comparison and Optimal Deformation of GBM Tumors

Figure 4 shows registration results for two simulated pre-shape + intensity objects. The data generating process for these simulated objects is described in Section S4 in the Supplementary Materials. In each panel, we display the two simulated tumor contours (labeled Shape) along with the corresponding intensity functions (labeled Intensity) in red and blue. The simulated contours have a round shape with one region of protrusion, and the size of the protrusion differs between the two contours. The corresponding simulated intensity functions have a single peak of high intensity with different magnitudes. For improved display, we plot the intensity functions as if they were defined on the domain *[0, 1]*. In Figure 4(a), we show the pre-shape + intensity objects. Recall that, to arrive at this representation, we (i)(center and) rescale the contours to unit length, and (ii) translate and rescale the intensity functions *via* subtraction of the mean and division by the standard deviation. In Figure 4(b), we show the registration result for a small value of $\lambda = 0.01$. In this case, the registration process is driven by geometric information of the contours as the protrusions on the two contours are well aligned. On the other hand, the peaks on the two intensity functions are misaligned since this information plays a minor role. When λ is increased to 0.5, as shown in Figure 4(c), intensity information dominates registration: the peaks on the intensity functions become well aligned while the protrusions on the contours become misaligned.

Figure 5 presents registration results for two pairs of T1 GBM tumors, which have visually similar (top row) and different (bottom row) shapes. The first pair shown in the top row come from subjects with survival times of 6.14 months (blue; subject 17) and 17.8 months (red; subject 23). In the bottom row, the tumors come from subjects with survival times of 42.1 months (blue; subject 57) and 14.3 months (red; subject 20). Similar to the registration results based on the simulated pre-shape + intensity objects (Figure 4), Figure 5(b) shows that when $\lambda = 0.01$, corresponding to very little emphasis on intensity information during registration, geometric features of the tumor contours are better aligned as compared to the intensity functions. When λ is increased to 0.5, the registration process focuses on intensity as demonstrated by improved alignment of the intensity functions in Figure 5(c).

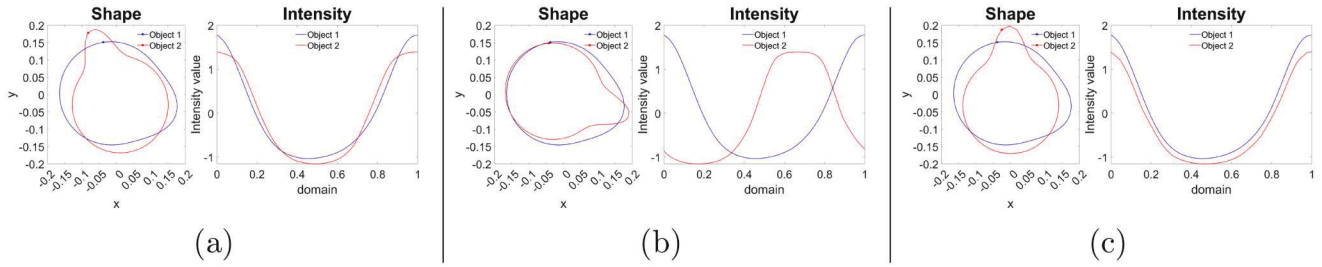

Figure 4. Registration of two simulated pre-shape + intensity objects. (a) Two pre-shape + intensity objects prior to registration. Registration results with (b) $\lambda = 0.01$, and (c) $\lambda = 0.5$.

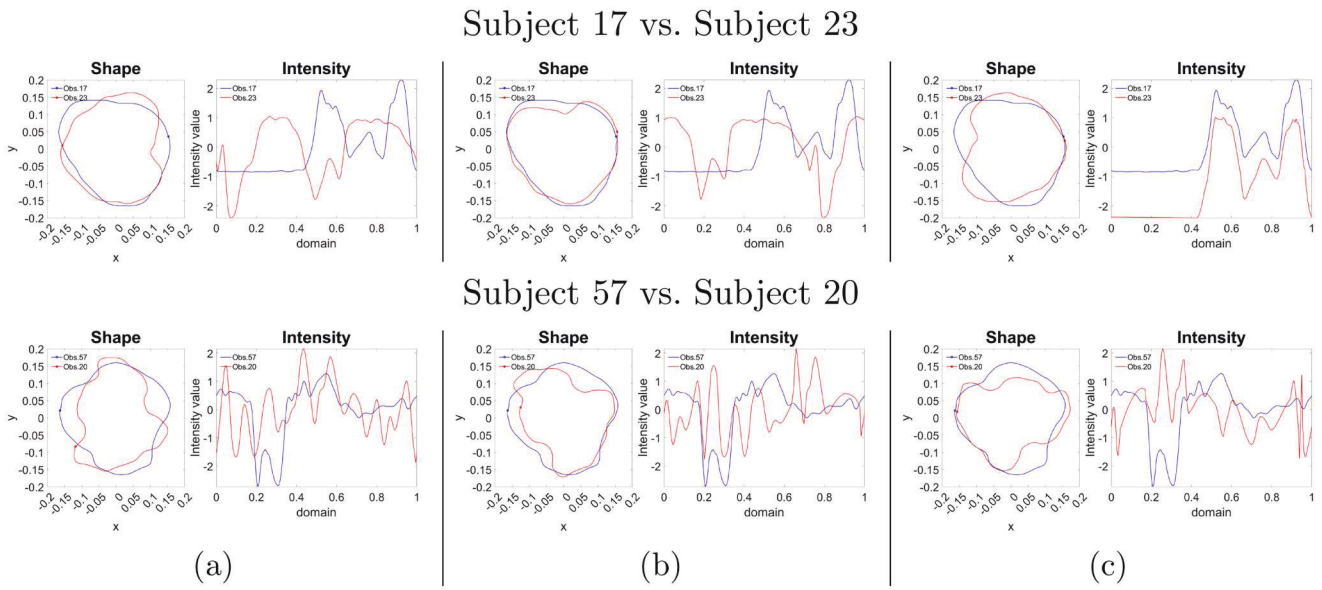

Figure 5. Registration of two pairs of T1 GBM tumor pre-shape + intensity objects that have similar (top row) and different (bottom row) shapes. (a) Pre-shape + intensity for two GBM tumors. Registration results when (b) $\lambda = 0.01$, and (c) $\lambda = 0.5$.

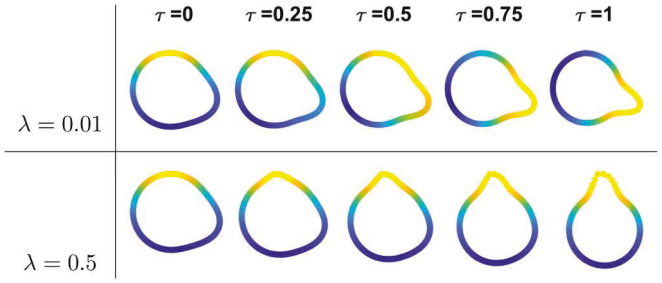

Figure 6. Shape + intensity geodesics between the two simulated pre-shape-+ intensity objects considered in Figure 3(a).

Figures 6 and 7 show geodesic deformations between the shape + intensity representations for the simulated example and two real T1 GBM tumor examples considered in Figures 4 and 5, respectively. These deformation paths were computed using Equation (7). Each row, from top to bottom, corresponds to a deformation computed with a different value of λ. Along each row, the geodesic path starts at the blue GBM tumor, followed by 5 equally spaced points along the path, and ends at the red one. Note that GBM tumor shape + intensity at the end of the geodesic path is optimally registered to the GBM tumor shape + intensity at the start of the path, based on the given value of λ. Along each geodesic path, shape components are drawn as 2D tumor contours with overlaid colors representing intensity. We do not include a colorbar indicating the scale of intensity values since they have been normalized prior to this analysis. As seen in the top row of each of the three figures, when λ is very small, the deformation is primarily driven by the shape component. Here, geometric features of the contours, e.g., protrusions, are in correspondence across the two shapes and this is reflected in the resulting geodesic path. As λ increases, the influence of the intensity component on the geodesic deformation becomes apparent. For instance, in the bottom row of each figure, when λ is large, we see that the deformation is mostly driven by the correspondence of high/low intensity values. Such deformations can provide valuable visualizations for clinicians as they assess severity of GBM based on imaging data.

3.2. GBM Tumor Shape + Intensity Heterogeneity by Sex

We first summarize the GBM tumor shape + intensity variation in the T1 MRI modality by sex *via* PCA for two different values of λ. The left and right columns of Figure 8 show the two primary directions (along rows) of shape + intensity variation when $\lambda = 0.025$, for females and males, respectively. Each PC direction is sampled at $-2, -1, 0, 1, 2$ standard deviations from the mean (see Equation (10)), i.e., the midpoint

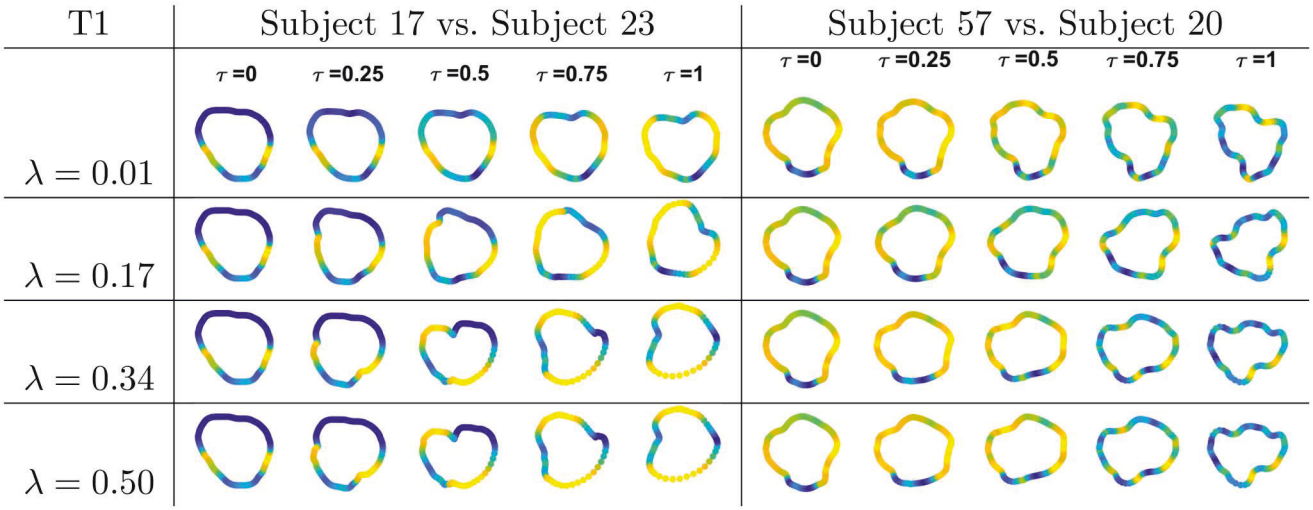

Figure 7. Shape + intensity geodesics (along rows), for different values of λ, between the T1 GBM tumors considered in Figure 5.

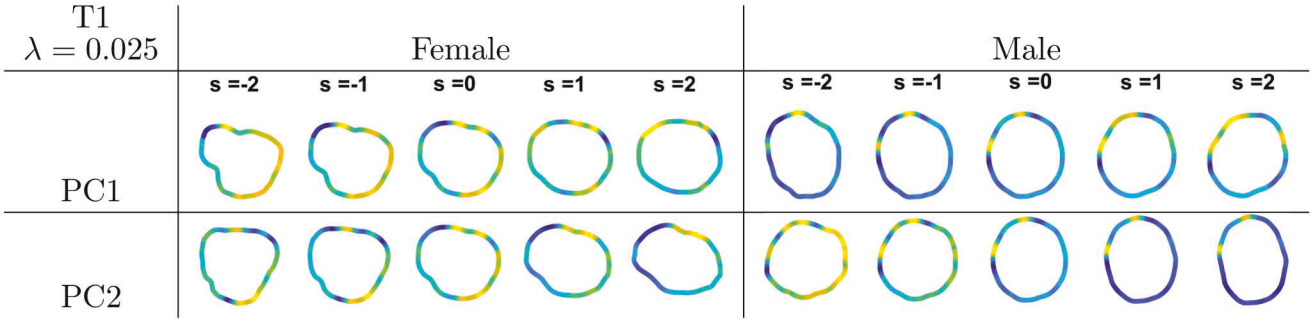

Figure 8. First two principal directions of variability around the mean, displayed along rows, for T1 GBM tumor shape + intensity in female (left) and male (right) subjects when $\lambda = 0.025$; $\hat{\rho}_{0.025,F} = 0.241$ and $\hat{\rho}_{0.025,M} = 0.254$.

of each path is the sample average computed *via* Equation (8). In this case, due to the small value of λ, the shape component dominates the analysis and the top principal components tend to capture more shape variation than intensity variation. Overall, T1 GBM tumor shape + intensity is more varied in the male group indicating higher tumor heterogeneity. The variances in the female and male groups are $\hat{\rho}_{0.025,F} = 0.241$ and $\hat{\rho}_{0.025,M} = 0.254$, respectively. The left and right columns of Figure 9 provide the same visualization of shape + intensity variation for females and males, but with $\lambda = 0.1$. We note the increased role of intensity information in these primary directions of variation. As before, overall variation in T1 GBM tumor shape + intensity is larger in the male group than in the female group: $\hat{\rho}_{0.1,F} = 0.549$, $\hat{\rho}_{0.1,M} = 0.582$

We repeat this process for FLAIR GBM tumor shape + intensity, with the same values of $\lambda = 0.025$ and $\lambda = 0.1$. These results are visualized in Figures 10 and 11, and similar conclusions can be drawn here as in the T1 MRI modality. As before, for each of the two values of λ, the overall variance in the male group is larger than in the female group. In particular, $\hat{\rho}_{0.025,F} = 0.401$ and $\hat{\rho}_{0.025,M} = 0.436$ when $\lambda = 0.025$, and $\hat{\rho}_{0.1,F} = 0.794$ and $\hat{\rho}_{0.1,M} = 0.850$ when $\lambda = 0.1$. It is also notable that there appears to be more variation in FLAIR GBM tumor shape + intensity than in T1 GBM tumor shape + intensity when the same value of λ is used for each modality.

Interestingly, previous studies have shown that females with GBM have longer median survival than males (Colopi et al. 2023; Ostrom et al. 2018). In our dataset, the sample median survival times for males and females are the same at 13.6 months, but the sample mean survival time is slightly longer for females than for males: 20.04 versus 17.84 months. Given the larger overall variance of GBM tumor shape + intensity in males than females, for both the T1 and FLAIR modalities, it appears that tumor heterogeneity, as captured by these features, provides valuable information about GBM prognosis. Alternative displays of the primary directions of variation shown in Figures 8–11, wherein the shape component is plotted separately from the intensity component, are provided in Section S9 in the Supplementary Materials. Also, bootstrap estimates of variance for the sample average shape + intensity in each sex group are provided in Section S5 in the Supplementary Materials.

3.3. Clustering of GBM Tumor Shape + Intensity and Survival Analysis

The proposed representation and distance can be incorporated into machine learning tasks, which can be useful in

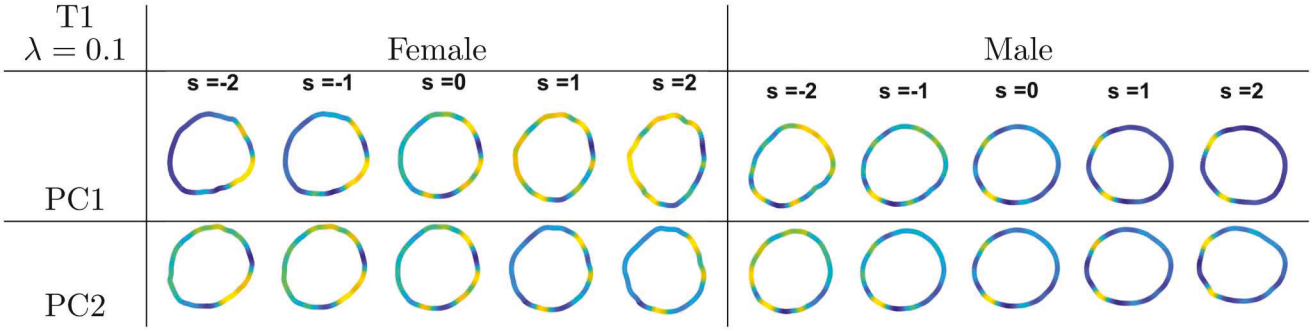

Figure 9. First two principal directions of variability around the mean, displayed along rows, for T1 GBM tumor shape + intensity in female (left) and male (right) subjects when $\lambda = 0.1$; $\hat{\rho}_{0.1,F} = 0.549$ and $\hat{\rho}_{0.1,M} = 0.582$.

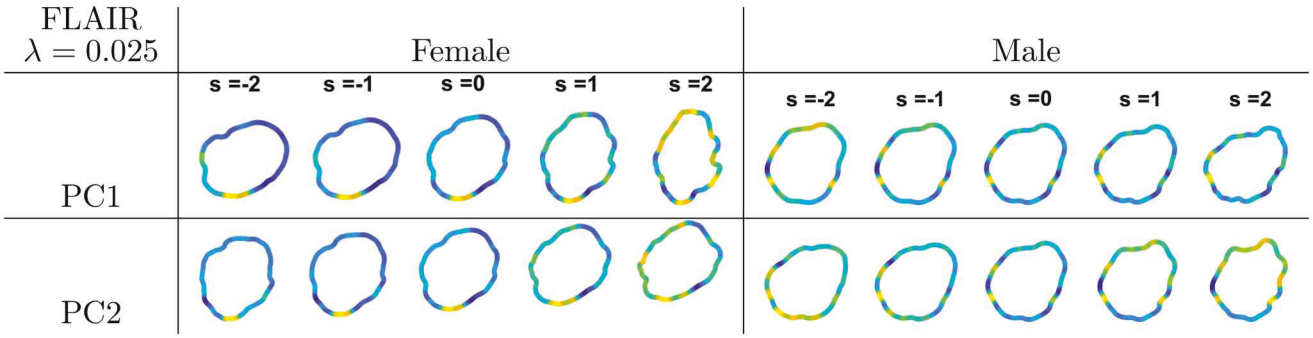

Figure 10. First two principal directions of variability around the mean, displayed along rows, for FLAIR GBM tumor shape + intensity in female (left) and male (right) subjects when $\lambda = 0.025$; $\hat{\rho}_{0.025,F} = 0.401$ and $\hat{\rho}_{0.025,M} = 0.436$.

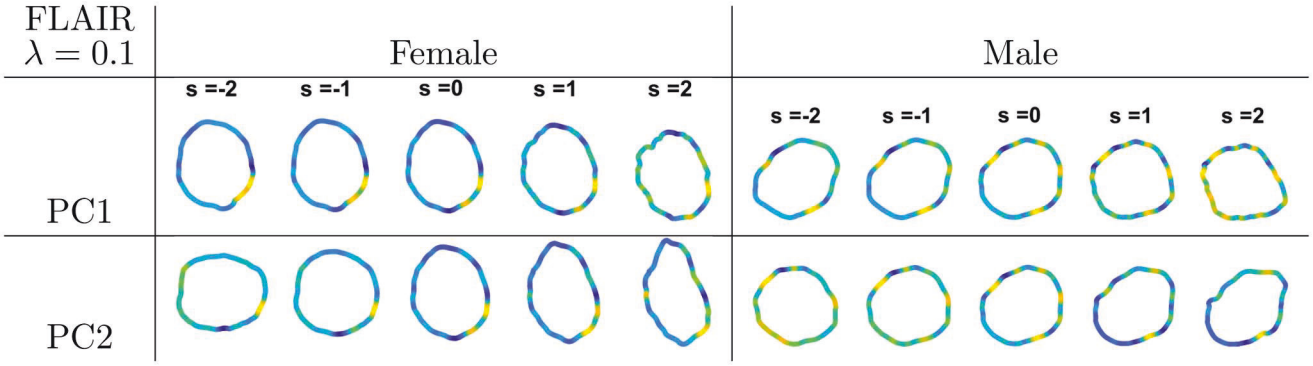

Figure 11. First two principal directions of variability around the mean, displayed along rows, for FLAIR GBM tumor shape + intensity in female (left) and male (right) subjects when $\lambda = 0.1$; $\hat{\rho}_{0.1,F} = 0.794$ and $\hat{\rho}_{0.1,M} = 0.850$.

assessing inter-subject GBM tumor heterogeneity with respect to shape and intensity features. In our analysis, we use distance-based hierarchical clustering to study differences in survival across partitions of the GBM tumor shape + intensity data. Depending on the choice of the tuning parameter λ, the clustering can be driven either by geometric shape differences (for small values of λ), intensity differences (for large values of λ) or both. Furthermore, if the composite distance defined in Equation (11) is used for clustering, the choice of the weight α additionally allows the clustering to focus more/less on differences in T1-derived or FLAIR-derived GBM tumor shape + intensity information.

We consider the entire dataset consisting of 63 subjects. For each subject, we have GBM tumor pre-shape + intensity extracted from T1 and FLAIR MRIs. For each modality, we first compute ten 63×63 pairwise distance matrices using Equation (6), corresponding to ten equally spaced values of λ between 0.01 and 0.5. Varying the parameter λ allows us to understand the importance of geometric shape versus intensity information in the clustering results and subsequent survival analysis. We then apply hierarchical clustering, with complete linkage, to each of the ten distance matrices and partition the data into two clusters, with the aim of discovering a value of λ that provides large separation between the clusters in terms of median survival. Our implementation uses the *linkage* and *cluster* functions in `MATLAB` (version R2022a).

First, in Figure 12(a), we display the absolute difference in median survival between the two estimated clusters for each value of λ and each MRI modality. In Figure 12(b), we show the corresponding absolute differences in the sample sizes across the two estimated clusters. For the T1 modality, the

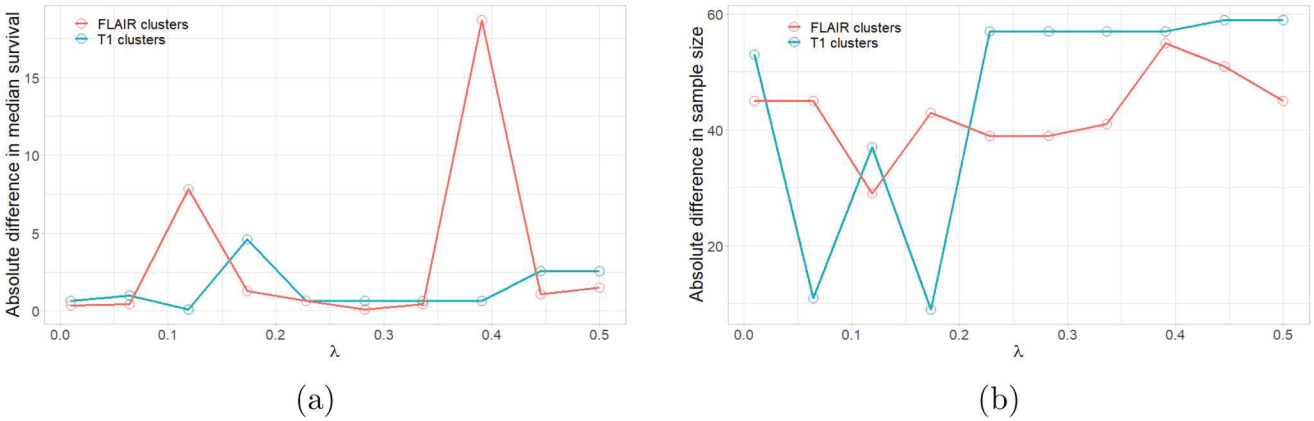

Figure 12. Absolute difference (*y* axis) in (a) median survival, and (b) sample sizes in estimated clusters for different values of λ (*x* axis). Results based on T1 data are shown in blue while results based on FLAIR data are shown in red.

largest absolute difference in median survival of approximately 4.6 months (cluster 1: median survival of 17.8 months with (95%) CI [10.4, 22.3]; cluster 2: median survival of 13.2 months with (95%) CI [6.87, 14.7]) occurs at a relatively small value of $\lambda = 0.17$, i.e., where shape plays a more prominent role than intensity in the comparison of GBM tumors. We also note that the two clusters are approximately balanced in terms of their sample size for this value of λ. For the FLAIR modality, the largest absolute difference of approximately 18.7 months occurs at a relatively large value of $\lambda = 0.4$, i.e., where intensity plays the dominant role in the comparison of GBM tumors. However, this difference may not be statistically reliable since one cluster contains only four subjects, yielding an absolute difference in the sample sizes across the two clusters of 55. On the other hand, when $\lambda = 0.12$, we discover two clusters that have sufficient sample sizes (more than ten observations in each cluster), and yield the second largest absolute difference in median survival of 7.85 months (cluster 1: median survival of 20.7 months with (95%) CI [6.14, 27.2]; cluster 2: median survival of 12.85 months with (95%) CI [8.8, 14.7]). Having sufficient sample sizes in both clusters for $\lambda = 0.17$ in T1 and $\lambda = 0.12$ in FLAIR suggests that the corresponding large differences in median survival discovered based on the proposed shape + intensity representation of GBM tumors are fairly reliable. However, whether or not having balanced sample sizes in the two groups of subjects with distinct survival is clinically relevant needs to be further investigated. Nevertheless, the corresponding survival differences based on the estimated clusters are quite large, as the median survival time in GBM is only 12 months (McLendon et al. 2008).

Figure 13 shows the clusterwise Kaplan-Meier estimates of survival probabilities for clusters estimated based on (a) T1 GBM tumor shape + intensity with $\lambda = 0.17$, and (b) FLAIR shape + intensity with $\lambda = 0.12$, i.e., the λ values that yield the largest absolute difference in median survival while having sufficient sample size in each cluster. In both cases, subjects placed in cluster 2 had lower survival probabilities across most of the study period. In particular, when clustering is based on the FLAIR modality, the difference in survival probabilities between the two clusters is larger across the study period and the Kaplan-Meier curves of the two clusters cross much later during the study period, as compared to clustering based on the T1 modality. This suggests that the FLAIR MRI-derived tumor shape + intensity may be more useful in identifying two groups of subjects with distinct survival patterns.

To again assess GBM tumor shape + intensity heterogeneity in the clusters computed using the value of λ that yields the largest difference in median survival, we display the clusterwise first two principal directions of variability for each of the two modalities in Figure 14 (T1) and Figure 15 (FLAIR). As before, each PC direction is sampled at $-2, -1, 0, 1, 2$ standard deviations around the sample average (see Equation (10)), which is the midpoint of each path. For the T1 modality with $\lambda = 0.17$, there appears to be little variation in terms of the shape of the tumors, especially in cluster 1. In cluster 2, we observe a lot of intensity variation along the first PC direction. The overall clusterwise variances in this case are $\hat{\rho}_{0.17,c1} = 0.648$ for cluster 1 and $\hat{\rho}_{0.17,c2} = 0.716$ for cluster 2. Interestingly, the GBM tumor shape + intensity in the T1 modality appears more heterogeneous in cluster 2, which was associated with shorter median survival. The clusterwise principal directions of variation, computed based on FLAIR GBM tumor shape + intensity with $\lambda = 0.12$ exhibit more shape and intensity variation than those computed based on the T1 modality. The resulting overall clusterwise variances in this case are $\hat{\rho}_{0.12,c1} = 0.751$ and $\hat{\rho}_{0.12,c2} = 0.855$ for cluster 1 and cluster 2, respectively. Again, GBM tumor shape + intensity is more heterogeneous in cluster 2, which is associated with shorter median survival. Alternative displays of the primary directions of variation shown in Figures 14 and 15, wherein the shape component is plotted separately from the intensity component, are provided in Section S9 in the Supplementary Materials.

Finally, Figure 16 shows multidimensional scaling (MDS)[4] plots (Borg and Groenen 2005; Cox and Cox 2001) for the shape + intensity data corresponding to (a) the T1 modality with $\lambda = 0.17$, and (b) the FLAIR modality with $\lambda = 0.12$. Each observation is colored according to its cluster membership (cluster 1: blue; cluster 2: red). In both panels, we see that there is reasonable separation between estimated clusters based on the proposed shape + intensity representation and distance, suggesting that the choice to partition the data into two clusters is appropriate in this setting. These plots further confirm that overall shape + intensity variation in cluster 2, which is

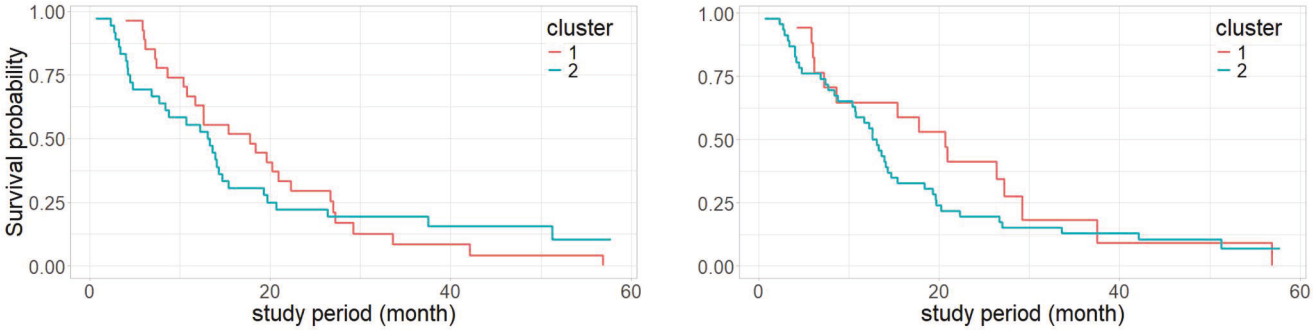

Figure 13. Clusterwise Kaplan-Meier survival estimates based on (a) T1 shape + intensity with $\lambda = 0.17$, and (b) FLAIR shape + inensity with $\lambda = 0.12$.

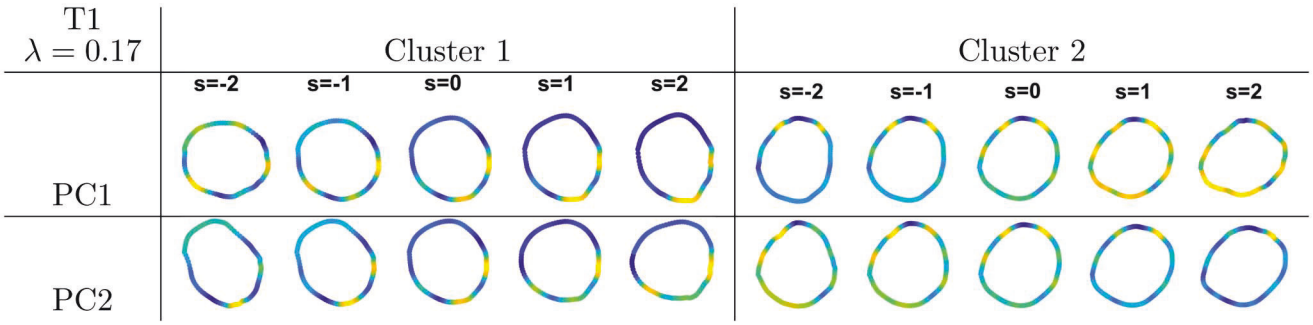

Figure 14. First two principal directions of variability around the mean, displayed along rows, for cluster 1 (left) and cluster 2 (right) estimated using T1 tumor shape + intensity with $\lambda = 0.17$; $\hat{\rho}_{0.17,c1} = 0.648$ and $\hat{\rho}_{0.17,c2} = 0.716$.

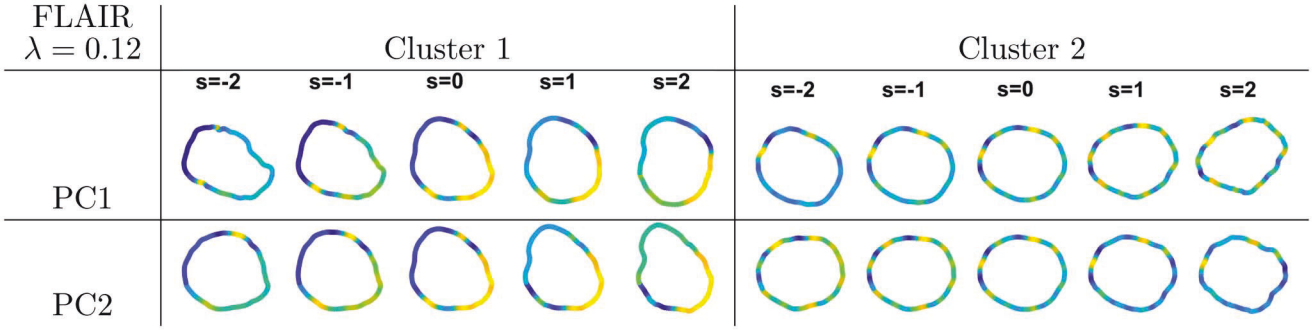

Figure 15. First two principal directions of variability around the mean, displayed along rows, for cluster 1 (left) and cluster 2 (right) estimated using FLAIR tumor shape + intensity with $\lambda = 0.12$; $\hat{\rho}_{0.12,c1} = 0.751$ and $\hat{\rho}_{0.12,c2} = 0.855$.

associated with shorter median survival, is larger than in cluster 1, for each MRI modality. Importantly, the MDS coordinates are computed using pairwise distance matrices only and do not incorporate survival information, i.e., it is a form of unsupervised dimension reduction.

In summary, the individual clusterings based on T1 and FLAIR GBM tumor shape + intensity both discover similar values of λ ($\lambda = 0.17$ for T1 and $\lambda = 0.12$ for T2) that yield a large difference in survival estimates across clusters with sufficient sample sizes. This indicates that GBM tumor shape is more informative relative to intensity information for identifying groups of subjects with distinct survival patterns. Moreover, we consistently find that the cluster associated with shorter median survival has more heterogeneous GBM tumor shape + intensity as measured by the overall variance.

To harness information from both modalities, we also perform clustering, again into two groups, using the composite distance defined in Equation (11) with three preselected values of the weight parameter $\alpha = 0.25, 0.5, 0.75$. As illustrated in Figure 17, this approach allows us to partition the data into groups that yield an even larger absolute difference in median survival while having sufficient sample size in each cluster. For instance, when $\lambda_1 = 0.01$, $\lambda_2 = 0.12$ and $\alpha = 0.5$, the difference in median survival between the estimated two clusters is 8.3 months (cluster 1: median survival of 20.9 months with (95%) CI [7.26, 27.2]; cluster 2: median survival of 12.6 months with (95%) CI [8.41, 14.3]) as compared to 4.6 months and 7.85 months when the T1 and FLAIR data are used separately. Moreover, as illustrated by the clusterwise Kaplan-Meier estimates of survival probabilities shown in Figure 18, the difference in the Kaplan–

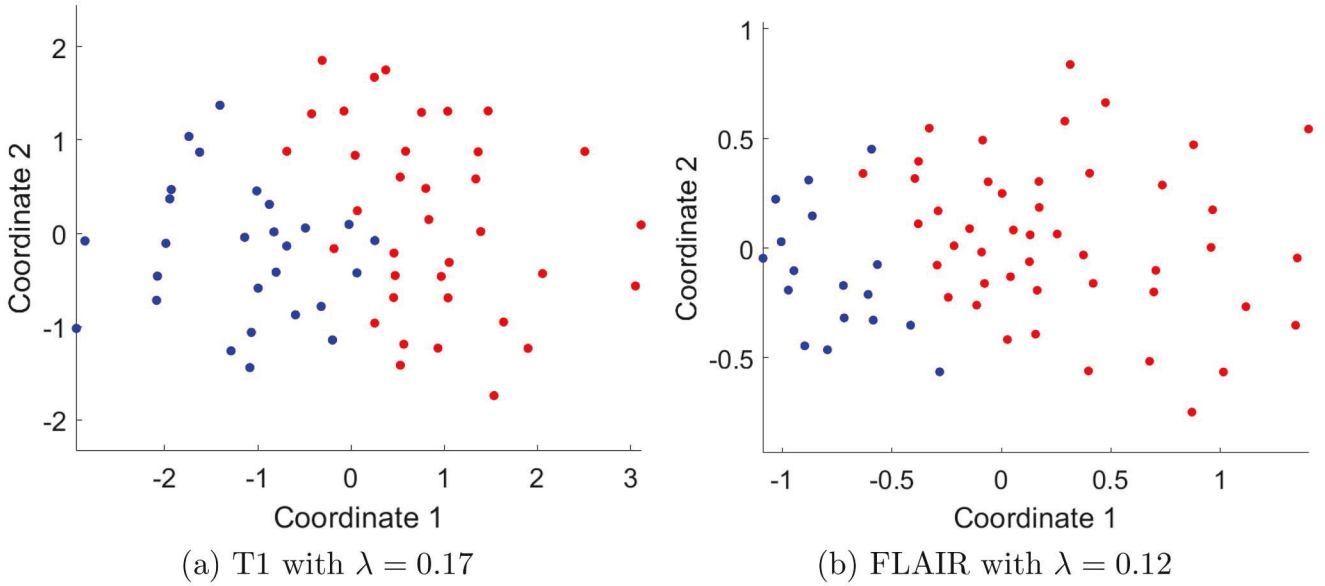

Figure 16. MDS plots, for λ values that yield largest absolute difference in median survival while having enough sample size in each cluster, for (a) T1 shape + intensity with $\lambda = 0.17$, and (b) FLAIR shape + intensity with $\lambda = 0.12$. Each subject is colored according to cluster membership: cluster 1: blue, cluster 2: red.

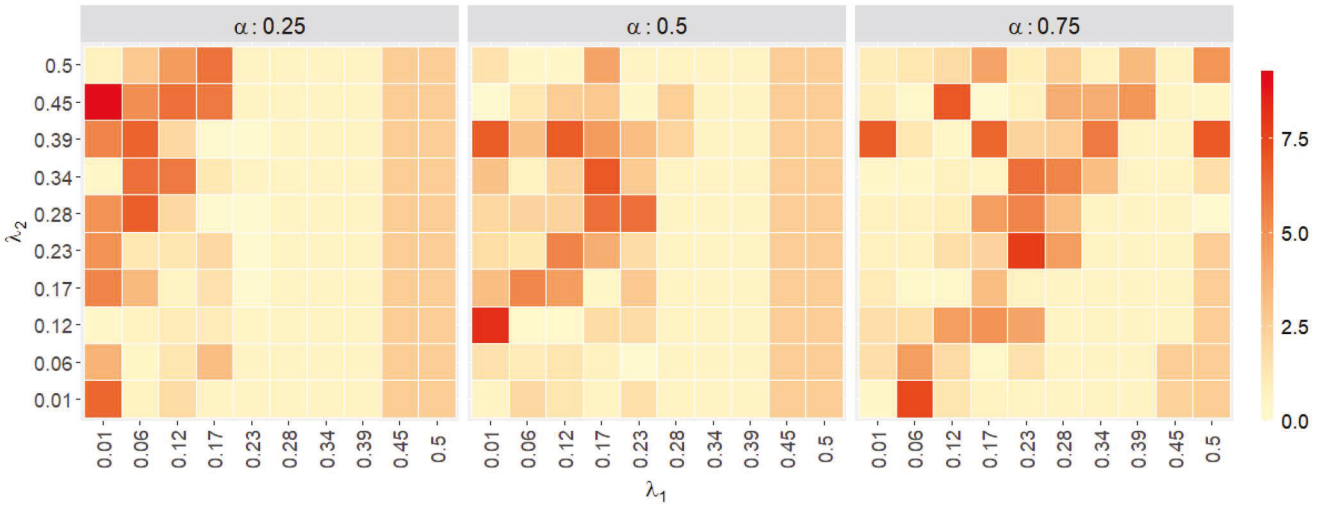

Figure 17. Absolute differences in median survival for different combinations of λ_1 (x axis), λ_2 (y axis), and α (panel). The parameters λ_1 and λ_2 control the emphasis on intensity information in T1 and FLAIR shape + intensity, respectively, while α controls the weight placed on each of the two modalities in the composite distance.

Meier estimates between the two clusters estimated using the composite distance is larger across the study period than those when T1 and FLAIR data are used individually (see Figure 13 for comparison). Large differences in median survival (red cells in Figure 17) mostly appear when $\lambda_1 \leq 0.23$, especially when $\alpha = 0.25,\ 0.5$, i.e., more emphasis placed on the shape component in the T1 modality. This further indicates the importance of the T1 GMB tumor shape component for discovering groups of subjects with distinct survival. This observation may be clinically relevant since the T1 modality captures the solid tumor area.

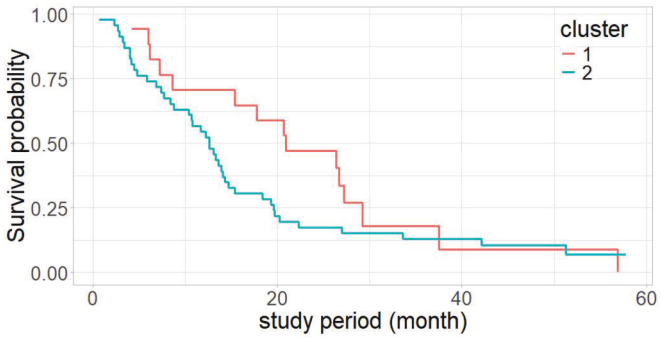

Figure 18. Clusterwise Kaplan-Meier survival estimates when $\alpha = 0.5, \lambda_1 = 0.01$, and $\lambda_2 = 0.12$.

3.3.1. Comparative Analyses

We compare the proposed integrated framework, which uses a joint shape + intensity representation and an associated distance, to alternative approaches which utilize (i) shape-only distances, or (ii) intensity-only distances. Our comparisons are based on hierarchical clustering and subsequent survival analysis as presented in Section 3.3. Note that the shape-only analysis is a special case of the proposed integrated

framework, i.e., specifying $\lambda = 0$ in the shape + intensity representation. Intensity-only analysis, on the other hand, is not a special case of the integrated framework, and thus involves a different representation and associated distance, which are presented in Section S7.1 in the Supplementary Materials.

Table 2 reports absolute differences in median survival where the clusters are estimated using shape + intensity, shape-only, or intensity-only distances. As seen in the table, for both T1 and FLAIR, the resulting absolute differences in median survival from using shape-only and intensity-only distances are smaller than those based on clustering using the shape + intensity representation and associated distance.

Tables 3–5 present absolute differences in median survival when clustering is based on the composite distance that utilizes shape + intensity, shape-only, or intensity-only information from T1 and FLAIR modalities, for $\alpha = 0.25$, 0.5 and 0.75, respectively. According to these tables, clustering based on the shape + intensity composite distance yields larger absolute differences in median survival while having sufficient sample sizes in the estimated clusters, as compared to those estimated based on clustering using shape-only or intensity-only composite distances.

Finally, in Section S7.2 in the Supplementary Materials we provide results of clustering based on a weighted combination of the shape-only and intensity-only distances within each modality. While this approach results in larger differences in median survival for some weights than the proposed integrated framework, the resulting clusters are highly unbalanced. On the other hand, using shape + intensity distance for clustering and subsequent survival analysis can yield clusters with sufficient sample sizes while having large differences in median survival as shown in Table 2. In summary, the comparative analyses presented here and in the Supplementary Materials demonstrate the benefits of using the proposed integrated framework for the task of discovering groups of subjects with distinct survival prognosis.

4. Discussion

We propose a framework that provides objective characterization and comparison of tumor shape and intensity, and allows assessment of tumor heterogeneity across subjects. The proposed representation combines and balances information about tumor shape and intensity along the tumor contour. The balance of information is achieved by scaling the intensity along the tumor contour to control its influence in the comparison and summarization of tumor shape and intensity information. The proposed representation and associated distance are invariant to translation, scale, rotation and reparameterization, which are desirable mathematical properties that lead to improved comparison of tumor shape + intensity. The proposed distance enables further

Table 2. Absolute differences in median survival based on clustering *via* the shape + intensity, shape-only, or intensity-only distances.

	T1		FLAIR	
Distance	Absolute difference in median survival	Sample size in smaller cluster	Absolute difference in median survival	Sample size in smaller cluster
shape + intensity $\lambda = 0.17$ for T1 $\lambda = 0.12$ for FLAIR	4.60	27	7.85	17
shape only $\lambda = 0$	4.35	10	0.90	12
intensity only	4.15	10	2.15	12

Table 3. Absolute differences in median survival based on clustering *via* a composite distance that utilizes T1 and FLAIR tumor shape- + intensity, shape-only, or intensity-only.

Distance	Absolute difference in median survival	Sample size in smaller cluster
shape + intensity $\lambda_1 = 0.06$ $\lambda_2 = 0.28$	6.80	22
shape only $\lambda = 0$	0.50	2
intensity only	4.95	4

The T1 and FLAIR tumor differences are weighted by $\alpha = 0.25$.

Table 4. Absolute differences in median survival based on clustering *via* a composite distance that utilizes T1 and FLAIR tumor shape- + intensity, shape-only, or intensity-only.

Distance	Absolute difference in median survival	Sample size in smaller cluster
shape + intensity $\lambda_1 = 0.01$ $\lambda_2 = 0.12$	8.3	17
shape only $\lambda = 0$	0.50	2
intensity only	1.95	12

The T1 and FLAIR tumor differences are weighted by $\alpha = 0.5$.

Table 5. Absolute differences in median survival based on clustering *via* a composite distance that utilizes T1 and FLAIR tumor shape- + intensity, shape-only, or intensity-only.

Distance	Absolute difference in median survival	Sample size in smaller cluster
shape + intensity $\lambda_1 = 0.06$ $\lambda_2 = 0.01$	7.45	26
shape only $\lambda = 0$	0.45	5
intensity only	4.35	3.

The T1 and FLAIR tumor differences are weighted by $\alpha = 0.75$.

statistical analysis of GBM tumor shape + intensity and can be easily integrated into machine learning tasks such as clustering and classification. Beyond the context of MRI-derived GBM tumors, the proposed approach is quite general and can be applied to data extracted from other medical imaging modalities.

We discover that a certain emphasis on the intensity component is helpful in distinguishing subjects with poor disease prognosis from those with good prognosis, in terms of survival, as shown in the clustering and survival analysis results. Furthermore, we are able to associate tumor heterogeneity, as measured by the overall shape + intensity variance, to differences in survival outcomes. Such information can aid medical decisions made by patients and clinicians after GBM diagnosis, e.g., whether to undergo invasive surgery to remove the tumor.

While we mainly consider the unsupervised learning task of clustering for discovering groups with distinct survival profiles, the proposed integrated framework can also be used in supervised learning tasks. An application to classification, wherein the parameters λ and α can be tuned automatically *via* cross-validation, is presented in Section S8 in the Supplementary Materials. In short, we discovered that using the composite distance with a k-nearest neighbors classifier, with large emphasis on shape differences in T1 and large emphasis on intensity differences in FLAIR, can better predict survival classes (as defined by a survival cutoff of 12 months) compared to using T1 or FLAIR shape + intensity distances separately.

We have identified multiple directions for future work. First, the proposed method uses information about the shape of the tumor outline and the intensity along the outline, which does not capture intensity information inside the tumor. A natural direction for future work is thus to extend the proposed approach to additionally use information about the level curves inside the tumor and the associated intensity values along these curves (Jermyn et al. 2012; Kurtek and Drira 2015; Portman et al. 2007). This extension can capture information about the spatial organization of intensity values inside the tumor, thus providing more information regarding GBM tumor heterogeneity. Second, we will develop survival models that are able to incorporate shape + intensity objects as predictors. This will enable inferential procedures that fully capture these MRI-derived GBM features. Third, most of the observations resulting from our statistical analysis are exploratory in nature and based on a relatively low sample size of 63 GBM subjects. We will thus apply the developed methods to a larger cohort for confirmatory purposes. Finally, we will use the proposed tumor shape + intensity representation in formal statistical models to study radiogenomic associations in the context of GBM (Mohammed et al. 2021, 2023).

Notes

1. http://cancergenome.nih.gov/
2. http://www.cancerimagingarchive.net/
3. The SRVF transformation actually flattens a single instance in the family of elastic Riemannian metrics by fixing the weights that penalize the bending and stretching/compression terms.
4. MDS is a useful tool for visualizing information about pairwise distances between objects in a lower dimensional space.

Acknowledgements

We thank Prof. Arvind Rao (University of Michigan) for providing the MRI data as well as collated covariate information used in this work.

Disclosure Statement

No potential conflict of interest was reported by the author(s).

Funding

This research was partially funded by Division of Computing and Communication Foundations [NSF CCF-1740761, NSF CCF-1839252], Division of Mathematical Sciences [NSF DMS-2015226], and National Institutes of Health [NIH R37-CA214955].

References

Baek HJ, Kim HS, Kim N, Choi YJ, Kim YJ. 2012. Percent change of perfusion skewness and kurtosis: a potential imaging biomarker for early treatment response in patients with newly diagnosed glioblastomas. Radiology. 264(3):834–843.

Bertsekas D. 1995. Dynamic programming and optimal control. Belmont: Athena Scientific.

Bharath K, Kurtek S, Rao A, Baladandayuthapani V. 2018. Radiologic image-based statistical shape analysis of brain tumours. J R Stat Soc Ser C Appl Stat. 67(5):1357–1378.

Borg I, Groenen PJF. 2005. Modern multidimensional scaling: theory and applications. New York: Springer.

Chaddad A, Desrosiers C, Hassan L, Tanougast C. 2016. A quantitative study of shape descriptors from glioblastoma multiforme phenotypes for predicting survival outcome. Br J Radiol. 89(1068):20160575.

Chen YT, Kurtek S. 2023. Shape and intensity analysis of glioblastoma multiforme tumors. In: Proceedings of IEEE Conference on Computer Vision and Pattern Recognition Workshops. p. 553–560.

Colopi A, Fuda S, Santi S, Onorato A, Cesarini V, Salvati M, Balistreri C, Dolci S, Guida E. 2023. Impact of age and gender on glioblastoma onset, progression, and management. Mech Ageing Dev. 211: 111801.

Cox TF, Cox MAA. 2001. Multidimensional scaling. Boca Raton: Chapman & Hall/CRC.

Dryden IL, Mardia KV. 2016. Statistical shape analysis: with applications in R. vol. 995. Chichester, UK: John Wiley & Sons.

Ellingson B, Zaw T, Cloughesy T, Naeini K, Lalezari S, Mong S, Lai A, Nghiemphu P, Pope W. 2012. Comparison between intensity normalization techniques for dynamic susceptibility contrast (DSC)-MRI estimates of cerebral blood volume (CBV) in human gliomas. J Magn Reson Imaging. 35(6):1472–1477.

Gevaert O, Mitchell L, Achrol A, Xu J, Echegaray S, Steinberg G, Cheshier S, Napel S, Zaharchuk G, Plevritis S. 2014. Glioblastoma multiforme: exploratory radiogenomic analysis by using quantitative image features. Radiology. 273(1):168–174.

Hawkins-Daarud A, Rockne R, Anderson A, Swanson K. 2013. Modeling tumor-associated edema in gliomas during anti-angiogenic therapy and its impact on imageable tumor. Front Oncol. 3:66.

Holland E. 2000. Glioblastoma multiforme: the terminator. Proc Natl Acad Sci USA. 97(12):6242–6244.

Jermyn I, Kurtek S, Klassen E, Srivastava A. 2012. Elastic shape matching of parameterized surfaces using square root normal fields. In: Proceedings of European Conference on Computer Vision. p. 804–817.

Just N. 2011. Histogram analysis of the microvasculature of intracerebral human and murine glioma xenografts. Magn Reson Med. 65(3): 778–789.

Karcher H. 1977. Riemannian center of mass and mollifier smoothing. Comm Pure Appl Math. 30(5):509–541.

Krabbe K, Gideon P, Wagn P, Hansen U, Thomsen C, Madsen F. 1997. MR diffusion imaging of human intracranial tumors. Neuroradiology. 39(7):483–489.

Kurtek S, Drira H. 2015. A comprehensive statistical framework for elastic shape analysis of 3D faces. Computers & Graphics. 51:52–59.

Kurtek S, Srivastava A, Klassen E, Ding Z. 2012. Statistical modeling of curves using shapes and related features. J Am Stat Assoc. 107(499): 1152–1165.

Liu W, Srivastava A, Klassen E. 2008. Joint shape and texture analysis of objects boundaries in images using a Riemannian approach. In: Proceedings of Asilomar Conference on Signals, Systems and Computers. p. 833–837.

McLendon R, Friedman A, Bigner D, Van Meir E, Brat D, Mastrogianakis G, Olson J, Mikkelsen T, Lehman N, Aldape K, et al. 2008. Comprehensive genomic characterization defines human glioblastoma genes and core pathways. Nature. 455(7216):1061–1068.

Mio W, Srivastava A, Joshi S. 2007. On shape of plane elastic curves. Int J Comput Vision. 73(3):307–324.

Mohammed S, Bharath K, Kurtek S, Rao A, Baladandayuthapani V. 2021. RADIOHEAD: radiogenomic analysis incorporating tumor heterogeneity in imaging through densities. Annals of Applied Statistics. 15(4):1808–1830.

Mohammed S, Kurtek S, Bharath K, Rao A, Baladandayuthapani V. 2023. Tumor radiogenomics in gliomas with Bayesian layered variable selection. Med Image Anal. 90:102964.

Nyúl LG, Udupa JK. 1999. On standardizing the MR image intensity scale. Magn Reson Med. 42(6):1072–1081.

Ostrom Q, Rubin J, Lathia J, Berens M, Barnholtz-Sloan J. 2018. Females have the survival advantage in glioblastoma. Neuro Oncol. 20(4):576–577.

Portman N, Grenander U, Vrscay E. 2007. New computational methods for the construction of "Darcyan" biological coordinate systems. In Proceedings of International Conference on Image Analysis and Recognition; vol. 4633. p. 143–156.

Robinson D. 2012. Functional data analysis and partial shape matching in the square root velocity framework [dissertation]. Tallahassee, FL: Florida State University.

Saha A, Banerjee S, Kurtek S, Narang S, Lee J, Rao G, Martinez J, Bharath K, Rao A, Baladandayuthapani V. 2016. DEMARCATE: density-based magnetic resonance image clustering for assessing tumor heterogeneity in cancer. Neuroimage Clin. 12:132–143.

Song Y, Choi S, Park CK, Yi K, Lee W, Yun T, Kim T, Lee SH, Kim JH, Sohn CH, et al. 2013. True progression versus pseudoprogression in the treatment of glioblastomas: a comparison study of normalized cerebral blood volume and apparent diffusion coefficient by histogram analysis. Korean J Radiol. 14(4):662–672.

Srivastava A, Klassen E, Joshi SH, Jermyn IH. 2011. Shape analysis of elastic curves in Euclidean spaces. IEEE Trans Pattern Anal Mach Intell. 33(7):1415–1428.

Srivastava A, Klassen EP. 2016. Functional and shape data analysis. New York: Springer.

Tutt B. 2011. Glioblastoma cure remains elusive despite treatment advances. OncoLog. 56(3):1–8.

Zinn P, Majadan B, Sathyan P, Singh S, Majumder S, Jolesz F, Colen R. 2011. Radiogenomic mapping of edema/cellular invasion MRI-phenotypes in glioblastoma multiforme. PLOS One. 6(10):e25451.